I&EC research

Industrial & Engineering Chemistry Research

Assessment of a Gas−Solid Vortex Reactor for SO$_2$/NO$_x$ Adsorption from Flue Gas

Robert W. Ashcraft, Jelena Kovacevic, Geraldine J. Heynderickx,* and Guy B. Marin

Laboratory for Chemical Technology, Ghent University, Krijgslaan 281 (S5), Ghent, B-9000, Belgium

S **Supporting Information**

ABSTRACT: The feasibility of performing the SO$_2$/NO$_x$ adsorption process in a gas−solid vortex reactor (GSVR) is examined and compared with the more traditional riser technology. The multiphase reacting flow is modeled using the Eulerian−Eulerian two-fluid model. Models of nonreacting flows were validated using data from a bench-scale experimental setup. The GSVR has the potential to significantly improved heat/mass transfer between phases, as compared to more conventional fluidization technologies. Process intensification opportunities are investigated. The model predicts continuous removal efficiencies greater than 99% for SO$_2$ and approximately 80% for NO$_x$. The gas−solid slip velocity and convective mass transfer coefficient for the riser were 0.2−0.5 and 0.06−0.12 m/s, respectively, whereas the values for the GSVR were 6−7 and 1.0−1.1 m/s, respectively. This order of magnitude increase in the external mass transfer coefficient highlights the potential intensification opportunities provided by the GSVR.

■ INTRODUCTION

The chemical process industry continually strives to achieve more efficient, precise, and cost-effective manufacturing of goods, and the process by which this is done is referred to as process intensification. Of the ways in which process intensification can be achieved, the two primary methods are optimization of the process or implementation of new and disruptive technologies that change the process, such as new reactor types or process chemistry. The focus of this work is a reactor type that is not new in the absolute sense, but is only recently being considered as a viable chemical reactor for traditional, high-volume industrial processes, such as petrochemical and energy conversion applications. This reactor type is known as a rotating bed reactor in a static geometry (RBR-SG), which can be implemented with several different phase combinations.

In addition to sporadic research efforts in the second half of the 20th century, the past decade has seen a relative resurgence in interest for RBR-SGs in several different fields, including nuclear technologies,[1,2] drying applications,[3,4] and chemical reactors.[5−7] This technology can be classified as a bed-type reactor that has hybrid characteristics of both fluidized bed and packed bed reactors. The unique attributes of the RBR-SG should allow it to significantly improve targeted industrial processes, particularly those that suffer from convective heat or mass-transfer limitations. In a gas−solid RBR-SG (henceforth called a GSVR), particles are made to rotate in a dense fluidized bed in a cylindrical reactor via the nominally tangential injection of a gas or gases through openings (slits in this example) in the curved outer wall of the reactor. The particles rotate in an annular-shaped bed which is forced toward the outer radius of the reactor by centrifugal force. One of the "end walls", or top and bottom of the cylinder, contains a central gas outlet and can be flat or curved. Momentum from the injected gas is transferred to the particles, causing the solids bed to rotate. The rotational motion induces a centrifugal force on the

particles, which counteracts the radial drag force created by the gas flowing from the circumferential inlet slits to the central outlet. The balance among the centrifugal force, the drag force, the various frictional forces, and the energy losses within the reactor is critical for the creation of a stable rotating bed of particles. If the drag force imparted by the gas flow overcomes the centrifugal force of the rotating particles, then particles will leave the bed with the gas through the central outlet. In the past decade, the fluid and particle dynamics in nonreacting flows have been studied by several researchers.[8−16]

In 1982, Paul B. Weisz succinctly described some interesting observations about production rates in the commodity chemical and petrochemical industries, in particular the fact that volumetric production rates generally fall in the range of approximately 1−10 mol/(m$^3_{reactor}$·s).[17] The lower end of the range stems from economic and availability arguments because low production rates are not (as) profitable and/or cannot meet demand. The upper limit is more interesting in this case because it typically arises from the inability to transfer mass or heat quickly enough to keep control of the process. The GSVR has ability to significantly increase interphase heat and mass transfer and may allow the "window" of achievable and practicable industrial rates to be increased.

An analogous unit to the GSVR is a standard rotating fluidized bed (RFB) with a rotating reactor, which should be acknowledged as both a competitor technology and as a source of information. A rotating fluidized bed reactor is a device where the reactor is mechanically rotated at high speeds to create the centrifugal force that opposes the fluid drag force. These reactors share many of the same operating principles as a GSVR, but with the added mechanical complexity that comes

with large moving parts. The RFB possesses most of the same advantages as a GSVR, including the ability to achieve large increases in heat and mass transfer. However, the RFB has one additional advantage above and beyond the GSVR: an RFB allows for independent setting of the gas flow rate and the rotational velocity, whereas these properties are inherently linked in the GSVR. The similar operating principles imply that much of the research on RFBs may be useful to understanding GSVR behavior.[13,18−21] However, the vast majority of research on standard RFBs has been focused on cold-flow understanding and measurements, as has been the case with GSVR technology.

Some important industrial processes requiring gas contact with solids include heterogeneous reactions using catalysts, scrubbing technologies using adsorbents, combustion of solid fuels, and pyrolysis/gasification of solids, e.g., coal and biomass. These processes are often performed using a fluidized bed or a packed bed of particles in the current technological paradigm. The properties and operational characteristics of a GSVR will allow it to overcome the inherent heat and mass transfer limitations of a traditional static (SFB) or circulating fluidized bed (CFB). In an SFB, the gas velocity (and thus the flow rate for a given reactor size) is limited because of the necessary balance between the drag force exerted by the gas on the particles and the gravitational force resisting the drag. In a CFB (or riser) this is not necessarily the case, but the particle slip velocity is limited to the terminal velocity for the simplest case of isolated particles. When particle clustering occurs, the slip velocity concept become more complicated because particles on the interior and exterior of clusters experience different environments. In this paper, the slip velocity (v_{slip}) is defined as the vector difference between the bulk gas-phase fluid velocity (v_g) and the particle solids velocity (v_s). The relatively small v_{slip} in traditional fluidized bed types also tends to limit the convective heat and mass transfer coefficients that regulate the transport processes at the particle scale. In a GSVR, the centrifugal force that opposes the fluid drag force can be much larger than the force of gravity, allowing a much higher v_g through the bed and resulting in larger v_{slip} values at the particle surface. The latter results in faster heat and mass transfer between the fluid and the particles and creates the potential for higher gas throughput per reactor volume, i.e., process intensification. In a packed bed situation, pressure drop and channeling are potential issues that limit flow rates and result in processing deviations. The dynamic, yet dense, nature of the GSVR particle bed may alleviate some of these concerns.

The GSVR literature is very limited in terms of the analysis of reacting flows, mainly because the nonreacting bed dynamics are still not fully understood. There are many industrial processes that utilize multiphase contact and that are potential candidates for GSVR implementation, but no specific chemical process has yet been proven to benefit from this technology. Several important industrial chemical processes that may benefit are adsorption processes, gas-phase polymerization, biomass pyrolysis, biomass/coal gasification, and fast catalytic partial oxidation of hydrocarbons. Very recently, one research group has performed a detailed computational study of fluid catalytic cracking in a GSVR[22] and an idealized analysis of combined pyrolysis and gasification of biomass in a GSVR.[23] These papers highlight two potential processes that could benefit from the technology and also briefly discuss the process intensification potential provided in each case. Adsorption of contaminants from exhaust gas streams and other process

effluents is an important industrial task, especially given the ever-more-stringent emission regulations in many countries. In this paper, the SO_2/NO_x adsorption process will be discussed in detail. In gas-phase polymerization to high-density polyethylene or linear, low-density polyethylene, the heat generated during the reaction is often a significant concern because if the growing polymer particle temperature rises above the glass transition temperature, the particles will agglomerate and cause severe reactor fouling. Reactant gases may be diluted to reduce reaction rates or other steps can be taken to remove heat from the reactor, such as injection and evaporation of liquid hydrocarbons.[24] The ability of the GSVR to increase convective heat and mass transfer to the particles (relative to conventional fluidized beds or risers) will allow for more heat to be dissipated and may potentially result in higher production rates. The efficient and economical utilization of biomass to produce thermal energy, electricity, high-value chemicals, and/or liquid or gaseous fuels is a goal of many researchers. Gasification or pyrolysis of biomass to fuels or chemicals is one application in which GSVR technology may provide specific benefits. Fast catalytic partial oxidation of hydrocarbons is a process that has been thoroughly researched in the past two decades using monolith, honeycomb, or foam-type reactions.[25−34] The potential applicability of GSVR technology is appealing because the reactor has the ability to provide a very short gas-phase residence time and large volume throughput.

This paper will be primarily concerned with a gas−solid RBR-SG, or a gas−solid vortex reactor (GSVR), but many of the principles discussed will be applicable to other phase combinations as well. The first section of the paper addresses computational fluid dynamic model validation with experimental data, and the second portion of the paper applies the model to the SO_2/NO_x adsorption process (SNAP). Discussion will focus both on the ability of the model to reproduce nonreacting experimental flow data and on the potential for this technology to be applicable to industrial processes, such as the SNAP. The GSVR shows the potential for significant process intensification, but a judicious choice of application will be critical to fully leveraging the unique attributes of the technology.

■ METHODOLOGY

The simulations presented in this work model the behavior of a GSVR unit that is similar in geometry to an existing experimental unit in the authors' lab, which is designed to examine nonreacting flows. The cylindrical outer manifold of the unit, through which the primary gas phase is introduced, has a diameter of 0.7 m. Inside the manifold, a series of 36 slits, 2 mm high, are arranged at a constant radius and at a constant 10° angle relative to the tangent of the cylinder. The result is an inner (active) reactor region with a diameter of 0.54 m in which the solid phase is contained. The total length (or thickness) of the reactor is 0.1 m. The volume of the reactor is defined as a cylinder with a diameter of 0.54 m and a height of 0.1 m, or 0.023 m^3. The main gas outlet is situated in the center of one end-wall (the other end-wall is a flat plate) of the reactor, and the total diameter of the central gas outlet is 0.15 m. After exiting the reactor, the gas flows into a cyclone, which is not relevant to the present work. Particles are introduced and removed through two approximately 1-cm holes in one of the reactor end-walls. This approach is experimentally observed to cause only minor disturbances in the particle flow and will be ignored in the simulations. A schematic representation of the
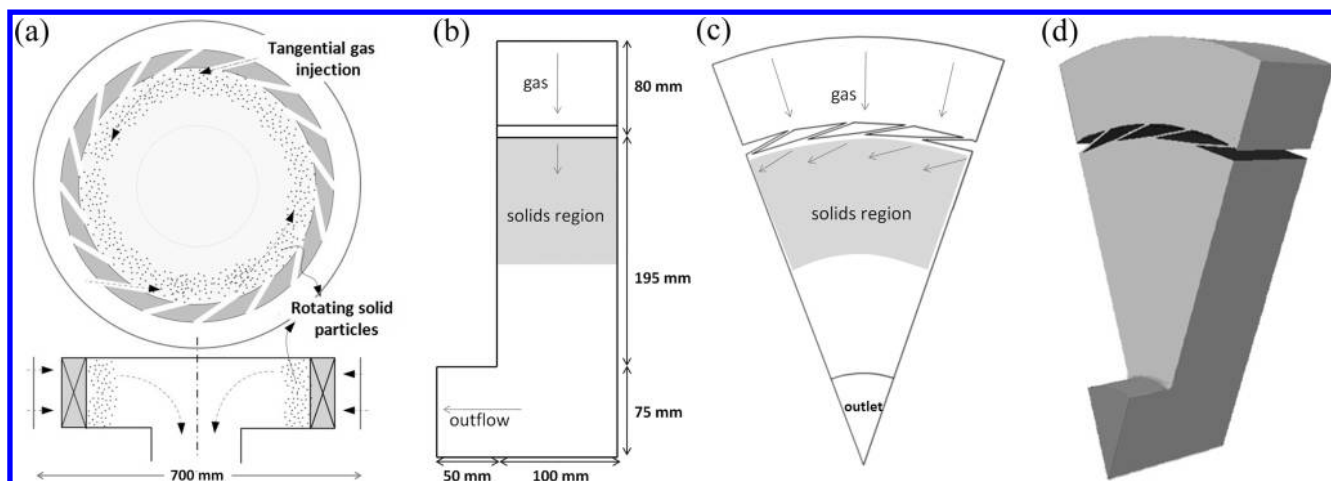
Figure 1. Schematic showing: (a) general side- and top-view illustration of the GSVR concept, (b) side-view perpendicular to the axis of rotation, (c) the end-view for a 40° section of the GSVR geometry (this is the primary geometry used in the CFD simulations), and (d) a 3-D schematic of the 40° section used in select CFD simulations.

reactor/computational domain is shown in Figure 1. The general region in which the rotating bed of particles typically resides is shown as the shaded region; the exact size of this region is of course dependent on the operating conditions, particle properties, and mass of solids in the reactor.

The behavior of the GSVR was analyzed using computational fluid dynamic simulations. The CFD software package FLUENT release 13.0 was used to perform the calculations, and the Eulerian–Eulerian granular solids formulation was employed to model the particle behavior. A nine-step lumped reaction model was used to model the adsorption process,[35] which will be discussed in more detail later. The GSVR simulations are then compared with riser simulations of the SNAP performed by Das et al.[35]

General CFD Model. The reactor was modeled with a 2D projection of 1/9th of the actual reactor using rotational periodic boundary conditions. This significantly reduced the computational cost of performing the simulations. The main consequence of this approach is that the gravitational forces have to be neglected. Both experimental data and simulations performed with a 360° geometry (not shown) confirmed that gravity had a minimal effect under the SNAP processing conditions tested. The 40° section was chosen because it seemed a reasonable trade-off between computational cost and domain size. Two-dimensional nonreacting flow simulations performed with a 360° geometry (not shown) confirmed that the primary observables (i.e., pressure drop, bed thickness, solids velocity, general bed structure) were nominally the same as with the 40° periodic section. The reactor was modeled using an unsteady, time-varying solver so that the dynamics of the bed could be captured. The time-varying simulations were performed in a series of steps: (1) flow gas only until a relatively stable flow pattern has developed (duration = 0.5 s), (2) begin to add the solids phase to create the desired bed mass of particles with reactions turned off (duration = 0.5 s), (3) turn off solids input and continue flowing gas only to create a stable bed of particles under nonreacting conditions (duration = 3 s), (4) if applicable, turn on the reactions and follow the changes in the bed dynamics until the unit achieves a dynamically stable operating state. The time required to reach steady-state operation varied depending on the operating conditions. For nonreacting flows, this typically required 10–30

s, whereas the SNAP modeling required 200–300 s due to the need to equilibrate the adsorbent surface species coverages.

Three computational domains were used in this work. The primary computation domain was the 2D, 40° periodic section mention earlier, which was meshed with approximately 12 500 cells varying in size from 0.5 mm near the gas injection locations to 4.0 mm near the outlet. A 2D, 360° geometry (~112 000 cells) and a 3D, 40° periodic section of the reactor (~270 000 cells) were also used to test the effect of model geometry on the simulation results. Results from these geometries are not discussed here, but the results for the primary observables were nominally the same as for the 2D, 40° periodic section. In general, the cell size was chosen to be smallest in the outer regions of the active reactor zone, where the solids generally reside and where the gas injections slits were located. These areas were mostly likely to involve dynamics on the smallest length and shortest time scales, and the small cell size there should capture the important flow phenomena. The distribution of cell volumes was such that 11% were below 0.5 mm^2, 31% were below 1 mm^2, 54% were below 2 mm^2, 71% were below 4 mm^2, 91% were below 10 mm^2, and 99.9% were below 16 mm^2. Simulations of nonreacting flows confirmed that time-averaged bulk properties as a function of radial position in the reactor, such as v_g, v_s, pressure drop (ΔP_{bed}), and solids volume fraction (ε_s), did not change significantly when the cell count was doubled. The simulations were performed on an AMD-based Linux cluster, and the typical wall time for a single time step with the 12 500-cell mesh was approximately 10 s using an 8-core CPU; therefore, achieving a dynamic steady state condition takes on the order of 250 days of CPU time.

Boundary conditions are critical parts of the simulations, and must be specified for inflows, outflows, and walls for both phases. The gas inlet velocity for the nonreacting simulations was specified to be 1.82, 2.73, or 3.64 m/s uniformly flowing through the outer manifold wall (@ $r = 0.35$ m), or equivalently, volumetric flow rates of 0.4, 0.6, or 0.8 m^3/s. This results in a gas "injection velocity" of approximately 55–110 m/s out of the 36 slits (2 mm × 100 mm). The outlet of the reactor is specified as a standard pressure outflow condition. The gas-phase wall boundary conditions are all no-slip conditions. The solid-phase wall boundary conditions were

specified using a specularity coefficient (ϕ), which is a measure of the tangential interaction or energy transfer between the solids phase and the wall. The specularity coefficient is part of the definition of the shear force of the granular phase at the wall ($\vec{\tau}_s$).[36,37]

$$\vec{\tau}_s = -\frac{\pi\sqrt{3}}{6}\phi\frac{\varepsilon_s}{\varepsilon_{s,\max}}\rho_s g_0 \sqrt{\Theta_s}\ \overrightarrow{U_{s,\|}}$$

In this equation, $\overrightarrow{U_{s,\|}}$ is the particle/wall slip velocity parallel to the wall, g_0 is the radial distribution function for the particles, Θ_s is the granular temperature of the particulate phase, and $\varepsilon_{s,max}$ is the solids volume fraction at maximum packing, i.e., 0.63 in this case. A large specularity coefficient implies a large degree of energy transfer between the solids and reactor wall, which essentially acts as a frictional force retarding the motion of the solid. Because the 2D geometry inherently does not account for the reactor end-walls, the end-walls are implicitly assigned a specularity coefficient of zero; however, the circumferential wall through which the slits pass at $r = 0.27$ m was assigned a value of 0.1. This value was chosen to yield reasonable agreement with the nonreacting, experimental ΔP_{bed} data discussed later. In the 3D simulations, a smaller specularity must be assigned to the wall (e.g., 0.05) because the effects of end-wall friction are included. Essentially, the specularity coefficient in the 2D case must be artificially high to compensate for the implicit lack of end-wall friction.

Additional details related to modeling parameters used in the CFD simulations are provided in the Supporting Information (SI).

Non-Reacting Flow Simulations. The gas phase in the nonreacting CFD formulation is treated as an incompressible ideal gas, and the viscosity is modeled using the two-coefficient Sutherland's Law with constants: $C_1 = 1.458 \times 10^{-6}$ kg/m·s·K$^{0.5}$ and $C_2 = 110.4$ K, which are typical coefficients for air at moderate conditions.[38] The viscous forces and turbulence are accounted for using the realizable k–ε model with standard wall functions, per-phase multiphase formulation, and the standard model constants provided by FLUENT.[39] All nonreacting simulations were isothermal and performed at 298 K.

The granular particle phase was assigned a density of 950 kg/m^3 with a uniform particle diameter of 0.0009 m, chosen to match the HDPE particles within our nonreacting experimental flow setup. The solids feed rate in the nonreacting simulations was chosen such that the final solids bed mass (m_{bed}) in the reactor was 2.12, 3.25, or 4.38 kg. This means that the maximum solids volume content in the active portion of the reactor ($r < 0.27$ m) was approximately 10–22% by volume, though the local ε_s was often much higher. The solids phase was treated as a granular phase, using the Gidaspow formulation for granular viscosity, the Lun et al. formulation for granular bulk viscosity, the Schaeffer formulation for frictional viscosity (with default parameters), an algebraic formulation for granular temperature, solids pressure and radial distribution by Lun et al., and a packing limit of 0.63.[38] To describe interactions between phases, the Gidaspow model[36] was used for drag, and the solid–solid restitution coefficient was taken to be 0.9, which is typical of HDPE.[40] Note that the Gidaspow drag model does introduce a discontinuity at a solid volume fraction of 0.2; however, this jump did not affect the bulk fluid dynamics in a significant way; i.e., the bulk bed behavior is similar to that observed when using continuous drag models.

SNAP Simulations. The gas phase for the SNAP simulation consisted of a dilute mixture of SO_2, NO, NO_2, and O_2 in N_2. The inlet SO_2, NO, NO_2, and O_2 concentrations were 1330, 531, 10, and 20 000 ppm by volume, respectively, with the balance being N_2. The gas inlet velocity was 2.73 m/s, which corresponds to 0.6 m^3/s or 0.495 kg/s when translated to the experimental setup. When combined with an m_{bed} of 5.38 kg, this represents the midpoint of the nonreacting validation matrix in terms of volume flow rate of gas and volume of solids in the bed. The diffusivities of the gas-phase species were determined by Fuller's semiempirical method utilizing atomic volumes,[41] and they were estimated to be 2.13×10^{-5}, 3.55×10^{-5}, 2.87×10^{-5}, 3.34×10^{-5}, and 3.36×10^{-5} m^2/s at 414 K for SO_2, NO, NO_2, O_2, and N_2, respectively. The viscosity of the gas phase was taken to be that of pure N_2 gas given the dilute nature of the impurities. Other gas properties were treated in the same manner as in the nonreacting flow simulations. All SNAP simulations were isothermal and performed at 414 K.

The solids phase in the SNAP simulations was considered to be an Al_2O_3-based sorbent with properties specified in previous papers.[35,42−44] The solids phase was composed of nine active surface species and one inert solid. The active surface site density was 0.928 mol$_{sites}$/kg$_{sorbent}$. It was assumed that adsorption occurs in the pores and does not increase the diameter of the sorbent particles. The particulate density of the fresh sorbent was 1550 kg/m^3, and the particle diameter was defined to be either 70 or 200 μm. The particle−particle restitution coefficient was taken to be 1.0 to match the riser simulations performed by Das et al.;[35] however, a brief sensitivity check determined that the bulk observables were minimally affected by changes in the restitution coefficient within a reasonable range. The other granular properties of the phase were taken to be the same as those described earlier in this paper. The m_{bed} in the SNAP cases was either 2.27 kg (direct riser comparison) or 5.38 kg (realistic operation) of adsorbent ($\rho_s = 1550$ kg/m^3).

The adsorption process was simulated in three modes of operations: (1) batch mode with no adsorbent feeding or removal after formation of the initial bed, (2) single-pass mode where fresh sorbent is fed to the reactor and an equivalent volume of partially spent sorbent is removed, and (3) recycle mode where fresh sorbent is fed at a given rate, partially spent sorbent is removed, and partially spent sorbent is recycled with a specified recycle ratio. The sorbent feed and removal rate was chosen such that the total bed volume remained constant, implying that the volumetric solids feed and removal rates were constant. The solids handling and regeneration portion of the process are not modeled here, and sorbent regeneration is assumed to be complete.

In batch-mode operation, a stable bed of sorbent particles is created under nonreaction conditions. Once a stable bed has been established, the reactions are turned on, and transient adsorption of the impurities was followed as a function of time. The breakthrough behavior and bed capacity were examined. However, batch mode does not represent a realistic mode of operations, which is why the following continuous-mode simulations were performed.

The single-pass, continuous operation mode is the simplest way to continuously operate the adsorption unit. Sorbent was fed near the inner edge of the 5.38 kg bed, between radial values of 0.20 and 0.21 m, and sorbent was removed at radial values between 0.260 and 0.265 m. The feeding and removal of

sorbent was accomplished by means of source and sink terms, not through the use of physical inlets and outlets in the model geometry; the two-dimensional nature of the geometry required the use of source/sink terms. However, the source and sink terms were active at locations in the reactor where physical solids feed and removal devices could be placed. The purpose was to use source/sink terms to feed and removal particles at reasonable locations in the reactor. Fresh sorbent, with all active surface sites free, was fed to the reactor at a rate of 0.103 kg/s. This feed rate was chosen to achieve the same ratio of gas flow rate to fresh sorbent (4.8 kg_{gas}/$kg_{sorbent}$) used in the riser simulations of Das et al. The sorbent removal rate was the product of the sorbent mass feed rate and the ratio of the spent sorbent density to the fresh sorbent density, thus enforcing a constant bed volume. Energy source and sink terms were included to ensure that the material was fed and removed at the operating temperature. The solids were assumed to enter the unit with zero momentum. A momentum sink term was added at the solids removal location, which effectively forced the solids to have zero momentum when exiting the reactor. Adding the momentum sink resulted in a 5−10% decrease in the v_s in the bed. A schematic of the continuous adsorption model used in the simulations is presented in Figure 2.
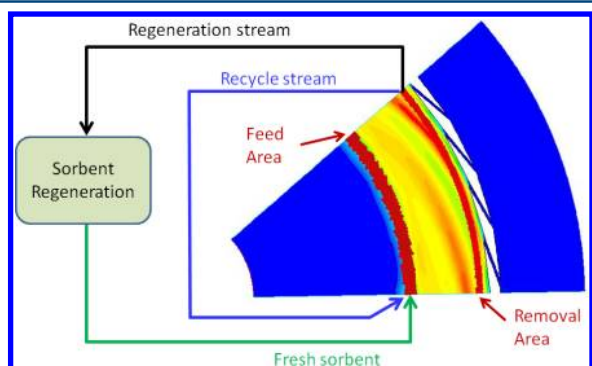

Figure 2. Schematic detailing the sorbent feeding and removal process in the simulations for the 5.38 kg bed. The source (feed) and sink (removal) areas are indicated and are located in the range of $r = 0.20$−0.21 m and $r = 0.260$−0.265 m, respectively. The contours are a representative snapshot of the solids volume fraction for the stable bed.

The continuous-recycle mode of operation was very similar to the single-pass mode. This mode is tested because the riser simulations included recycle. The recycle mode was used in two simulation cases: a direct comparison with the riser with m_{bed} = 2.27 kg and a more realistic operational case with m_{bed} = 5.38 kg. The feed/removal locations for the 5.38 kg case were the same as in the one-pass case, whereas the feed and removal locations in the 2.27 kg case were at radial positions of 0.24−0.245 and 0.26−0.265 m, respectively. The revised feed locations retain the concept of feeding near the inner edge of the bed. In these cases, sorbent was removed from the bed at a larger rate, and a portion of the sorbent removed was regenerated to yield fresh sorbent, and the remaining sorbent was recycled in the as-removed state. The recycle ratio, defined as the mass ratio of recycled sorbent to regenerated sorbent, used in this work was 3:1. In the simulations, there was no delay between the removal of the sorbent and its reintroduction into the unit. The effect of recycle is discussed later in the paper. When recycling sorbent, the coverage-dependent

kinetics become more complicated, which is discussed briefly in the SNAP kinetics section and in detail by Das et al.[35] These complexities were treated in a manner consistent with that of Das et al.[35]

SNAP Reaction Chemistry. The reaction chemistry was chosen to be as simple as possible while capturing the important characteristics of the SNAP. The reaction mechanism and kinetic parameters used in the simulations were from Das et al.;[35] however, additional information can be found in several other papers by Das et al. and De Wilde et al.[42−44] A summary of the most salient aspects of the mechanism and kinetic parameters is provided here, and the reader is referred to the aforementioned references for an in depth derivation and analysis of the kinetics. The reaction mechanism and the rate coefficients at 414 K are provided in Table 1. The species that are in braces in the table indicate species that participate in the reaction, but are not specifically included in the rate expression for that reaction. The number of sites occupied by the product of the reaction is provided in the table to provide a sense of the size of the adsorption complex formed in each reaction. This number was determined by Das et al. through a fitting of experimental data and varying the stoichiometry of reaction 5.[42] In general, the rate expressions are the product of the rate coefficient, the gas-phase species concentrations (if applicable), and the surface species fractional coverage. The free surface site fraction that appears in the rate expression is modified to account for the coverage-dependent nature of the rates.[35] The kinetic model was implemented in the same manner as in the riser simulations of Das et al.,[35] and the reader is referred to that paper for additional details. The rate constants are defined in such a way that the rate expression yields units of mol per mol_{site} per second, which can then be multiplied by the site density (0.928 mol_{site}/$kg_{sorbent}$) and the local catalyst bulk density ($kg_{sorbent}$/$m^3_{reactor}$) to arrive at a volumetric reaction rate.

The effect of external mass transfer between the gas phase and the sorbent particles was accounted for in the reaction rate expressions, although in general these reactions are kinetically limited under the GSVR conditions studied. The form of the net rate expression was derived by assuming that the mass-transfer rate to the particle surface was equal to the consumption rate within the particle.

■ EXPERIMENTAL VALIDATION OF NON-REACTING FLOWS

As mentioned previously, the authors' group operates a GSVR capable of investigating bed behavior and operational properties in nonreacting flows. This apparatus is described in more detail elsewhere.[45] Although the present computational results cannot be fully validated using reacting flow experiments, it is worthwhile to determine how effectively CFD simulations of nonreacting flows reproduce experimental data. The primary experimental variables that are accessible are the apparent bed thickness (H_{bed}), the ΔP across the reactor or bed, and the v_s near the end-wall (when a high-speed, high-resolution camera is used). In the current setup, there is only access to H_{bed} and ΔP measurements, which also provide data related to average bed ε_s via the known m_{bed}.

The experimental H_{bed} determinations were carried out by feeding quasi-spherical high-density polyethylene (HDPE) particles at a known feed rate of 12.5 g/s into the GSVR unit. The HDPE particles can be described as rounded cylinders with an approximate effective diameter of 0.9 mm

Table 1. Reactions and Intrinsic Rate Coefficients for the SNAP Simulations[35]

	reaction	sites occupied by product	rate coefficient (414 K)	notes
1.	$SO_2 + (*) \rightarrow SO_2^*$	1	4.73	b
2.	$NO_2 + (*) \rightarrow NO_2^*$	1	2.36	b
3.	$SO_2^* + (*) \rightarrow SO_2^{**}$	2	3.08	c
4.	$NO + O_2 + SO_2^{**} \rightarrow [NO_2SO_3]^* + (*)$	1	2105	d
5.	$[NO_2SO_3]^* + \left\{ 3SO_2^*, \frac{3}{2}O_2 \right\} \rightarrow R_t^{4*}$	4	0.0685	c,f
6.	$R_t^{4*} + O_2 + \left\{ \frac{1}{2}O_2 \right\} \rightarrow R_s^{4*}$	4	0.099	b
7.	$NO_2^* + SO_2 + \{2SO_2\} \rightarrow NO + [O(SO_2)_3]^*$	1	2.02	b
8.	$R_t^{4*} + NO_2 \rightarrow 2NO + 4O_2 + Q^{4*}$	4	1.73	b
9.	$NO + \frac{1}{2}O_2 + (*) \rightarrow NO_2 + (*)$		0.64	e

[a]Free reactive surface sites are indicated by (*). [b]$m^3 \, mol_{site}^{-1} \, s^{-1}$. [c]$mol \, mol_{site}^{-1} \, s^{-1}$. [d]$m^6 \, mol^{-1} \, mol_{site}^{-1} \, s^{-1}$. [e]$m^{4.5} \, mol^{-0.5} \, mol_{site}^{-1} \, s^{-1}$. [f]This rate coefficient was reduced by a factor of 1000 due to a typographical error in the reported value in the referenced publications. See the electronic Supporting Information for a detailed explanation.

and a density of 950 kg/m^3. As the solids were being fed, visual measurements of H_{bed} were collected, including the average thickness, as well as the minimum and maximum thickness due to natural fluctuations in the bed. Several runs were performed for each process condition to ensure reproducibility of the measurements. Measurements were taken for feeding times of 3, 4.5, and 6 min, which correspond to total m_{bed} values of 2.13, 3.25, and 4.38 kg, respectively. The standard deviation in m_{bed} was determined to be approximately 3% based on comparison of physical measurements of m_{bed} and the solids feed rate of 12.5 g/s. It was also confirmed that solids losses from the unit were negligible for the m_{bed} values examined here; significant particle losses began to occur with m_{bed} greater than 4.75 kg. Air flow rates of 0.4, 0.6, and 0.8 m^3/s were used in the study, which translate to air mass flow rates of approximately 0.49, 0.73, and 0.98 kg/s based on an air density of 1.22 kg/m^3.

Because this paper is not meant to be a detailed analysis of experimental work, only a cursory presentation of the data that is relevant to the CFD model validation will be provided. Experimental pressure data were collected at 6 points in the GSVR: (1) in the inlet manifold upstream of the injection slots, (2) at the circumferential wall between two injection slots, $r = 0.27$ m, (3) at $r = 0.255$ m, (4) at $r = 0.24$ m, (5) at $r = 0.21$ m, and (6) at $r = 0.15$ m. These measurement locations allow for independent verification of the pressure across the bed, the pressure drop across the inlet slots, and the total pressure drop; however, ΔP_{bed} is most relevant to the model validation. The pressure data constitutes the average over 30 s after the unit has reached a stable condition, which occurs within tens of seconds after feeding has stopped.

The experimental data were compared with nonreacting CFD simulations with the same m_{bed} and gas flow rate. The CFD data used to determine H_{bed} for the comparison was the ε_s as a function of radial position, where the ε_s data had been averaged over the final 0.5 s of simulation time and over the cylindrical azimuthal coordinate. This type of average should yield a similar representation of what would be observed visually by looking at the bed profile through the end-wall. The computed averaged ε_s varies smoothly from the zero in the freeboard region to the main bed zone, typically over a distance of 20–30 mm. This smoothing is due to a combination of the

inherent smoothing provided by the two-fluid model and the spatial/time averaging of fluctuations that are predicted to occur naturally within bed. H_{bed} for the simulations was defined using the radial value at which the ε_s was 0.05. The bed pressure drop based on the simulation data was determined using the pressure along the circumferential wall at location similar to where the experimental pressure was obtained. The simulated ΔP_{bed} was computed by averaging over 0.5 s of data.

Figure 3 presents a graphical comparison of the experimental and computational ΔP_{bed} and H_{bed} data. As noted earlier, the specularity coefficient was adjusted to achieve agreement between the experiment and computational ΔP_{bed} for the 0.74 kg/s air flow rate and $m_{bed} = 3.25$ kg data point. H_{bed} is also in good agreement at these conditions, though adjustments were not made to force agreement of this observable. Close
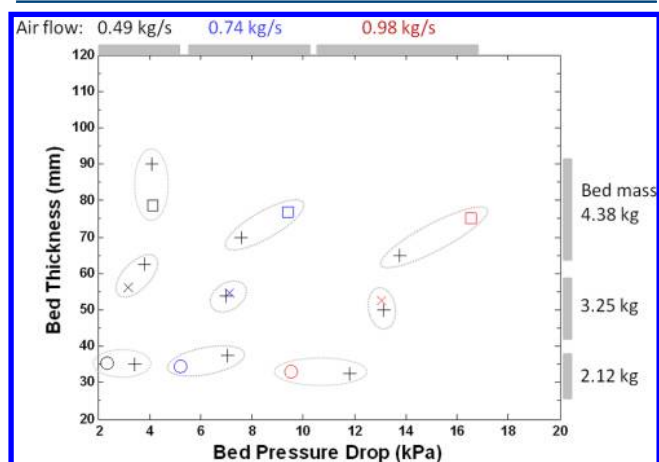

Figure 3. Comparison of bed thickness and bed pressure drop for experimental data (+) and CFD simulations (○: 2.12 kg bed, ×: 3.25 kg bed, and □: 4.38 kg bed). The leftmost "column" of data corresponds to an air flow rate of 0.49 kg/s, the middle corresponds to 0.74 kg/s, and the rightmost corresponds to 0.98 kg/s. The ovals enclosing the data aid in visual matching of corresponding experimental and computational pairs. Error bars are not included, but typical 95% confidence intervals in the experimental bed thickness and pressure drop are 10% and 2%, respectively.

Table 2. Independent Basis Variables and Quantities Derived from the Independent Variables for the Riser and GSVR Cases

	riser	GSVR simulation cases			
		direct riser comparison	5.38 kg bed no recycle	5.38 kg bed with recycle	batch operation
Independent Basis Variables					
reactor volume (m^3)	24.2	0.023	0.023	0.023	0.023
total gas feed flow rate (kg/s)	4.84	0.495	0.495	0.495	0.495
regenerated solids feed rate (kg/s)	1.01	0.103	0.103	0.103	
recycle ratio (kg$_{recyc}$/kg$_{regen}$)	3	3		3	
solids hold-up (kg)	22.0	2.27	5.38	5.38	2.27 or 5.38
Derived Quantities					
gas-to-regenerated solids (kg$_{gas}$/kg$_{regen}$)	4.8	4.8	4.8	4.8	
gas-to-total solids fed (kg$_{gas}$/kg$_{solids}$)	1.2	1.2	4.8	1.2	
space-time (kg$_{solids}$·s/mol)^a	68	69	160	160	69 or 160
weight hourly space velocity (1/h)^b	2.8	2.8	1.2	1.2	2.8 or 1.2
solid residence time (s)^c	22	22	50	50	22 or 50
solids loading (kg/m$^3_{reactor}$)	0.9	100	230	230	100 or 230
gas−solid contact time (s)	4.1	∼0.005	∼0.01	∼0.01	∼0.005 or 0.01

^{a}Space−time is defined as the mass of solids in the reactor divided by the inlet molar flow rate of contaminants. ^{b}WHSV is defined as the inlet mass flow rate of contaminants divided by the mass of solids in the reactor. ^{c}Solids residence time is defined as the solids loading divided by the regenerated solids feed rate.

agreement is obtained for the 3.25 kg case, whereas errors become more pronounced as the gas flow rate increases and at the higher and lower m_{bed}. There are several possible explanations for the discrepancy between the experimental and computed pressure drop. The first is that the experimental pressure measurement location and the computed pressure are not precisely equivalent. The experimental upstream pressure was measured with a tube inserted through the outer wall between two injection slots. In an attempt to be consistent, the CFD upstream pressure was defined as the pressure on a section of the outer wall between two inlet slots. However, the pressure calculated by CFD varies strongly in the region around the injection slots. For example, for the 4.38 kg bed and 0.98 kg/s air case, the pressure changes by ∼8 kPa as one moves along the outer wall from one injection slot to the next. A second potential explanation is that the drag model used in the work is not sufficient to describe the pressure drop as a function of solids volume fraction and/or flow rate through the bed under these high-centrifugal-force conditions. This is discussed in more detail in the following paragraph.

The comparison shows several distinct trends in the data. First, at low gas flow rates and higher m_{bed}, H_{bed} tends to be under-predicted by the CFD simulations. This effect is particularly evident in the 0.49 kg/s + 4.38 kg case and is directly attributed to the influence of gravity. Full 2D, 360° simulations with the gravitational force included showed the ability to capture this increase in thickness at low flow rates and high bed masses. The second trend is the clear propensity of the simulations to underestimate ΔP_{bed} at a low m_{bed} and to overestimate ΔP_{bed} at a high m_{bed}. This behavior is clearly seen at the 0.74 and 0.98 kg/s air flow rates. This effect is believed to be caused by more fundamental deficiencies in either the two-fluid model or in the key gas−solid interaction models, such as the applied drag law. The continuum nature of the two-fluid model implies that it is not capable of resolving small-scale behavior, such as particle clustering, that could significantly affect the bed behavior and pressure drop. The Gidaspow model used to calculate the fluid/solid momentum interaction coefficient (β), or drag, in this work provides different equations for low and high ε_s. Under the conditions studied,

the second term in the Gidaspow model is dominant. This term is proportional to the ε_s multiplied by v_{slip} and accounts for 75–90% of the drag under typical GSVR conditions. This linearity of β with respect to ε_s means that the product of the dominant drag term and H_{bed} is effectively independent of ε_s and primarily depends on the m_{bed}. Therefore, even though the average ε_s decreases as m_{bed} increases, m_{bed} has a very strong influence on ΔP_{bed}, whereas ε_s has only a minor influence. For example, the values of $\beta \cdot H_{bed}$ are approximately 290, 440, and 600 kg/(m^2·s) for m_{bed} = 2.13, 3.25, and 4.38 kg, respectively, whereas the typical ε_s values were 0.55, 0.50, and 0.45. It is not a coincidence that the ΔP_{bed} and $\beta \cdot t_{bed}$ scale similarly with m_{bed} in the CFD simulations. The experimental data indicate that the real-world dependence of ΔP_{bed} on m_{bed} is different from that indicated by the applied drag model. The exact reason for the deficiency is unclear, though it could be a combination of the drag model and the continuum nature of the two-fluid model. Although additional drag models from Syamlal et al.,[36] Benyahia et al.,[46] and Beetstra et al.[47] were tested, the Gidaspow model was found to yield the best results for these unique, high-centrifugal-force operating conditions. It is beyond the scope of this paper to attempt to derive a new drag model, but it may be a useful future task that could yield improved GSVR simulations. However, the Gidaspow drag model and other computational settings provide sufficient accuracy required for the scope of this paper, as will be demonstrated in the nonreacting flow validation results.

■ RESULTS AND DISCUSSION

The discussion here will focus mainly on the performance of the GSVR relative to the riser, and will not address the fundamentals of the SNAP outside of where those fundamentals are relevant to GSVR operation. All riser data used for comparative purposes and all references to Das et al. relate to the SNAP simulations in a riser published in 2004.[35] Explicit reference will be made from here onward only when data from other sources is mentioned.

It is important to examine the relevant operational conditions of the two technologies compared in this paper. The most pertinent ones are summarized in Table 2 for the riser, batch
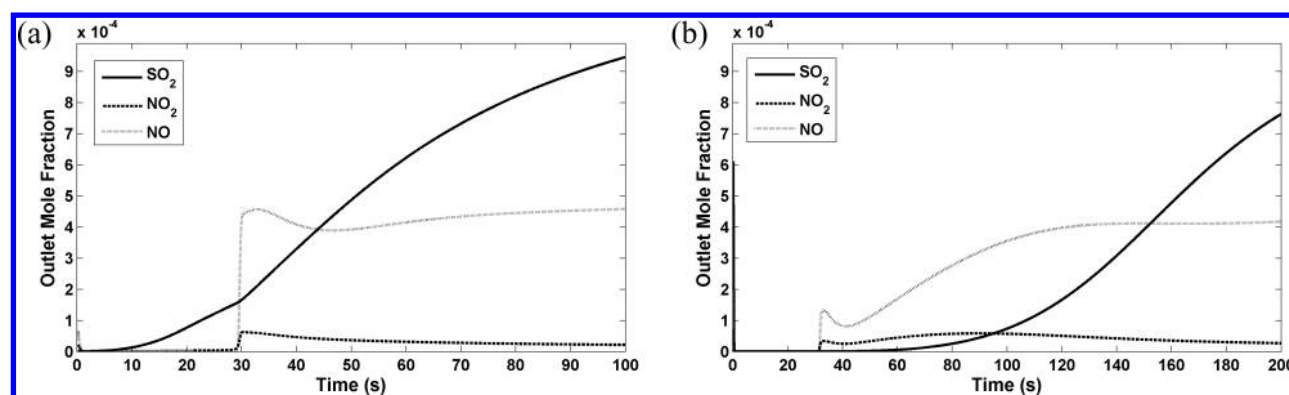
Figure 4. Time-varying outlet mole fractions for batch adsorption in a GSVR. (a) Batch adsorption with a 2.27 kg bed mass. (b) Batch adsorption with a 5.38 kg bed mass.

GSVR, GSVR without recycle (fresh sorbent only), and both GSVR cases with recycle. To be consistent with the experimental GSVR setup, the size of the computational GSVR model was not scaled to achieve an equivalent gas flow as the riser. Approximately 10 GSVRs would need to be operated in parallel to treat the same amount of gas processed in the riser. Because of this, several processing variables were kept constant in the riser/GSVR comparison.

The process can be described in terms of a minimum basis set of independent operational variables, assuming a constant reactor geometry and constant temperature. Useful derived process variables can also be defined to aid in the understanding of the process. The independent variables in the basis set for the GSVR are the following: (1) gas feed flow rate, (2) fresh sorbent feed rate, (3) sorbent recycle ratio, (4) solids hold-up or loading, and (5) gas feed composition. Some of the useful derived quantities based on the independent variables are the gas-to-solids feed ratio, space−time, weight hourly space velocity, gas or solids residence time, and gas−solid contact time. The derived quantities are those that are kept constant during a comparison because they are intensive variables, which are important because the volumes of the riser and GSVR are different. The relevant dependent variables in the GSVR are the pressure, solids velocity, gas velocity, solids volume fraction, and species concentration fields.

The most important process attribute was the ratio of the gas flow rate to the fresh sorbent feed rate. The fresh sorbent feed rate to the GSVR was chosen to achieve a gas-to-regenerated solids ratio of 4.8, identical to that in the riser simulations. The second conserved variable in the direct comparison case was the average solids residence time, which is defined as the solids hold-up divided by the fresh sorbent feed rate. Additionally, the weight hourly space velocity (WHSV) for the direct comparison case was the same in the riser and GSVR simulations; therefore, the solids loading per unit of gas flow is equivalent. When the GSVR was simulated with sorbent recycle, the recycle ratio was chosen to be equivalent to that used in the riser simulations. The GSVR with sorbent recycling can be considered a direct analogue to the riser unit, except that it processes approximately 1/10th the gas flow of the riser. Given that the important observables are intensive properties, the total throughput has minimal relevance in this modeling study, where scale-up is assumed to be accomplished through numbering up as is typical in process intensification. Scale-up issues will be a concern when attempting to implement a large GSVR-based process in industry.

In addition to the operational parameters that were conserved in the comparison, there are also notable differences that highlight the potential benefits of the GSVR. First, there is the large difference in the reaction zone volume, which is approximately a factor of 100 smaller in the GSVR per unit mass of gas processed. The reason for this large difference is because the GSVR operates with an ε_s between 0.1 and 0.6, whereas a typical value of ε_s in the riser was 0.0004 in the bulk flow and 0.001 near the walls. The ability of the GSVR to operate with a very dense particle bed also manifest itself in the volumetric solids loading, which was 100−230 $kg/m^3_{reactor}$, compared to a value of only 0.9 $kg/m^3_{reactor}$ for the riser. The final key difference is the gas−solid contact time, which is on the order of 10 ms for the GSVR due to the relatively thin bed and high radial gas velocity ($v_{g,r}$). When considering the 4.1 s contact time for the riser, the high conversions remain achievable in the GSVR because the volumetric reaction rates are typically proportional to the local bulk density of the catalyst, which is approximately 100 times larger in the GSVR. Short gas−solid contact times may also provide secondary benefits, such as the ability to reduce unwanted side reactions. For example, if there are undesired, noncatalytic, gas-phase side reactions occurring alongside a catalytic/adsorption process, then a short overall reactor residence time could provide a means of controlling the reactions that are not dependent on the catalyst bulk density. Alternatively, if the process relies on gas-phase reactions, then this could be a fundamental limitation. This highlights the fact that a GSVR may not be beneficial for all processes but has the potential to significantly improve ones that leverage the attributes of the technology.

Batch Adsorption In a GSVR. Although batch adsorption is not the optimal operational mode, simulating this mode can provide a general behavioral profile of the process and elucidate the time scales of the dynamic phenomena occurring in the process. This simulation was performed with both m_{bed} = 2.3 and 5.3 kg to allow comparison of a more realistic solids loading and the direct riser comparison. Based on the inlet gas flow rate and composition, the ideal bed capacity and breakthrough time can be estimated. The brief analysis that follows is based on the 5.38 kg bed, though it can be easily scaled to a different m_{bed}. The 5.38 kg bed contains approximately 4.9 mol of active sites and can capture an equivalent amount of impurities if one assumes that each active site is capable of capturing one SO_2 or NO_x molecule. The inlet gas flow rate is 17.6 mol/s, which translates to SO_2 and NO_x feed flow rates of approximately 23.5 and 9.5 mmol/s,

respectively. If the adsorption process were 100% efficient and all active sites could be filled, then the sorbent would be saturated and breakthrough of impurities would occur after approximately 150 s. Due to the rapidly decreasing effective free site fraction as adsorption occurs, the rate of adsorption and apparent capacity drop significantly. An additional complication in the GSVR is that the bed is dynamic, and does not behave like a fixed bed. The bed in the GSVR more closely resembles a well-mixed solids bed. This mixing behavior results in more smoothly changing outlet concentrations, not the relatively abrupt change one may expect in a highly efficient fixed bed. Therefore, the initial increase in impurity concentrations at the outlet will be observed before the ideal time of 150 s, and the apparent bed capacity will be reduced because of the exponential decay in the reaction rates as the surface coverage increases.

The observed simulation data confirm the above supposition. The time-varying concentration profiles of SO_2, NO, and NO_2 are presented in Figure 4 for both bed masses. The initial breakthrough of NO and NO_2 occurs at approximately 30 s for both bed masses. Equivalent breakthrough times for different m_{bed} values may seem counterintuitive, but this phenomenon is due to the kinetics of the reaction pathway. The spike in outlet NO can be attributed to the processes occurring during the adsorption process (see Table 1). (1) Some NO is oxidized to NO_2, which is then quickly adsorbed by the fresh sorbent. (2) The fast adsorption of SO_2 and the plentiful free surface sites at early reaction times results in rapid SO_2^{**} production. The high availability of SO_2^{**} means that NO can adsorb efficiently via reaction 4. (3) As the sorbent saturates and the number of free active sites drops, the rate of reaction 4 drops because SO_2^{**} is now being produced at a slower rate. (4) At the same time, the rates of reactions 7 and 8, which produce NO, continue to increase as surface species produced earlier in the reaction pathway make their way through the reaction chain. (5) The O_2 concentration also increases at the same time as NO, which is consistent with a decrease in the rate of reaction 4 and an increase in the rate of reaction 8. The NO_2 concentration generally follows the behavior of NO due the oxidation reaction. The SO_2 concentration in the outlet rises more gradually due to the more favorable adsorption kinetics and because it is not a product of any reaction. Therefore, the equivalent breakthrough times for the NO_x species are mainly determined by the characteristic time of the reaction pathway leading to reactions 7 and 8 and due to the solids mixing that transports the surface species to the downstream end of the bed.

Direct Riser Comparison for a GSVR with Sorbent Recycle. A GSVR with fresh sorbent feed and sorbent recycle is the most direct analogue to the riser reactor, which also included sorbent recycle. This particular case used a solids loading (2.27 kg) that achieved values very close to those of the riser for the gas–solid contact time, the gas-to-solids feed ratios, and the WHSV. Simulations of a GSVR with sorbent recycle were performed in the same manner as the GSVR without recycle, discussed in the next section. The results of the simulations, shown in Table 3, are similar to the riser results but were significantly worse than the GSVR case discussed later (with a 5.38 kg bed). The GSVR achieves slightly better removal of SO_2, with 119 ppm-v in the outlet compared to 122 ppm-v for the riser. Removal of NO is significantly better, with the GSVR outlet gas containing only 84 ppm-v, compared to a value of 128 ppm-v for the riser.

Table 3. Comparison of SO_2 and NO_x Removal for the Riser and GSVR Simulations

| | | | outlet gas composition (ppm-v) | | |
| | | | GSVR simulations | | |
species	inlet	riser	direct riser comparison, 2.27 kg	5.38 kg bed mass no recycle	5.38 kg bed mass with recycle
SO_2	1330	122	119	3.3	3.6
NO	531	128	84	81	85
NO_2	10	28	29	29	30
NO_x	541	156	113	110	115
O_2	20 000	18 795	19 070	18 952	18 956
SO_2 removal		90.8%	91.0%	99.7%	99.7%
NO removal		76%	84%	85%	85%
NO_x removal		71%	79%	80%	80%

The similarity of the results for the riser and the GSVR direct comparison case is generally expected because of the similar solids loading relative to the gas flow rate, which implies that the space–time and WHSV are the same for the two reactors. Under these conditions, there are two main factors that allow the GSVR to achieve slightly better results. (1) Improved mass transfer implies that the reaction is more kinetically controlled in the GSVR. Mass-transfer effects are more prevalent in the riser and result in a lower apparent reaction rate. (2) The reactor-scale gas–solid contact in the GSVR is more efficient due to the dense bed and uniform gas flow. In the GSVR, both the particulate phase and the gas flow through the particulate phase are relatively uniform, helping to optimize gas–solid interactions and preventing gas bypass. In the riser, the v_g is highest, and ε_s is lowest, near the centerline of the riser, which means that a large fraction of the gas flow (the core gas flow) does not interact with the significant portion of the solids that resides near the wall. For example, ∼80% of the gas flow in the riser (located in the core of the riser at $r < 0.8R$) contains only ∼60% of the solids, which implies that this portion of the gas will react at a slower rate than implied by the average flow rate and average ε_s.

The GSVR compares favorably to the riser in the direct comparison, but this set of operational conditions is significantly suboptimal for the GSVR. More specifically, the solids loading in the GSVR can be 2–3 times larger than the amount used in the direct comparison case, which will allow for a similar increase in the space–time. This will allow the reaction to reach a higher conversion. One benefit of the GSVR is that the solids loading can be set independently of the gas flow rate, the recycle ratio, or the fresh sorbent feed rate, until the maximum m_{bed} is reached for a given set of conditions. The primary penalty for increasing m_{bed} in the GSVR is an increased ΔP_{bed} and potentially a decrease in bed stability, particularly if m_{bed} approaches the maximum stable m_{bed}. This is not possible in the riser because the loading is completely determined by the gas and solids feed rates and momentum transfer between phases. The riser solids loading can be increased by decreasing the gas flow rate or increasing the recycle ratio, with the primary penalties being lower throughput or additional pressure drop, respectively. Of course, there are complex, nonlinear fluid dynamic effects that could be important when changing operational conditions.

Because the direct comparison case represents suboptimal GSVR operation, the majority of the remaining discussion will
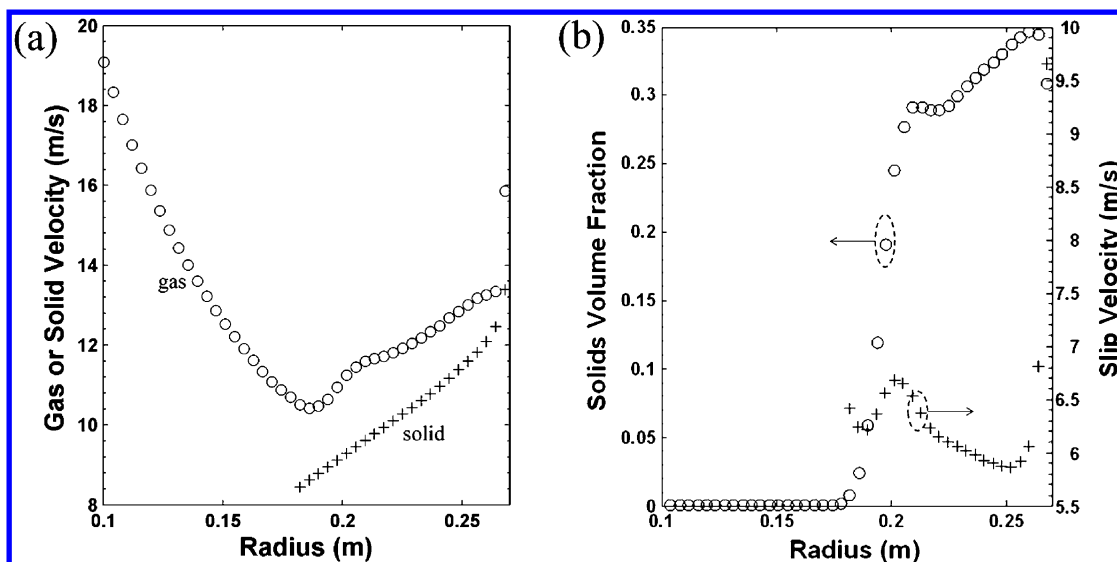
Figure 5. Steady-state GSVR operational data for the 5.38 kg bed, single-pass case. (a) Gas (O) and solids (+) velocities as a function of radius. (b) Solids volume fraction (O: left axis) and gas–solid slip velocity (+: right axis) as a function of radius.

focus on a more realistic solids loading for the GSVR (5.38 kg). This choice was not meant to represent the optimum conditions for adsorption. In a practical sense, the most important operational condition associated with the sorbent is the fresh sorbent feed rate because it is associated with the rate of regeneration. Having additional solids loading would represent a negligible cost relative to the regeneration and other operating costs. The higher-mass bed also makes for a more illustrative example because the bed is thicker and radial variations in the parameters are easier to present. The thicker bed also implies that any injection slot effects will be dampened more than for thinner beds.

Adsorption in a GSVR with a 5.38 kg Bed and without Sorbent Recycle. The adsorption process without sorbent recycle is the simplest continuous process that could be realistically implemented. Fresh sorbent is fed, spent sorbent is removed and regenerated, and then the regenerated sorbent is fed to the unit again. As presented in Table 2, the GSVR model without recycle shares many of the important processing conditions with the riser simulation. In the continuous operation cases, the only concern was the steady-state operation and performance of the unit. The steady-state condition was said to be reached when average species mole fractions were changing at a rate less than 0.01% per second, for both gas-phase and surface species.

The gas-phase velocity, solids-phase velocity, solids volume fraction, and gas–solid slip velocity are all important operational characteristics of the GSVR. Simulation data for these parameters during steady-state operation are presented in Figure 5. The raw data were averaged over the cylindrical azimuthal coordinate and over 0.5 s of simulation time, resulting in time-averaged data that are a function of the radial position in the GSVR. The gas injection occurs at a radial position of 0.27 m; therefore, the net gas flow is effectively from right-to-left as presented in the graphs. This matches the orientation of the GSVR geometry as presented in Figure 2.

Figure 5a presents the magnitudes of v_g and v_s. Note that the solids bed is present between $r = 0.175$ and 0.27 m. The gas velocity is relatively high near the outer wall of the GSVR due to the high injection velocity, but v_g decreases quickly due to

momentum transfer to the bed and the large increase in available flow area. The v_g is ~14 m/s at large radial values, ~11 m/s at the inner edge of the bed, and increases to near 22 m/s in the freeboard region as it flows to the outlet. As the gas moves across the bed, its velocity decreases further due to slowing of the tangential component as more momentum is transferred to the solids phase. The radial velocity ($v_{g,r}$) increases due to the inward radial flow, but the increase is not enough to counteract the continued slowing of the tangential velocity ($v_{g,t}$). Once the gas flow exits the bed, v_g increases in a manner that conserves angular momentum, i.e., $v_g \cdot r$ is approximately constant (~1.9 m²/s in this case). The v_s varies from ~13 m/s near the outer wall to ~9 m/s at the inner edge of the bed. Essentially all of the solids velocity magnitude comes from the tangential component, as should be the case in a stable bed. In the bulk of the bed away from the injection slots, the tangential velocities of the gas and solids phases are approximately equal, and the tangential v_{slip} is typically less than 0.1 m/s. The solids velocities in this case equate to centrifugal accelerations of 460 and 725 m/s² at radial positions of 0.175 and 0.27 m, respectively.

Figure 5b presents the average ε_s and v_{slip} as a function of radius. The average ε_s in the majority of the bed is between 0.30 and 0.40, and H_{bed} is between 0.08 and 0.10 m. The instantaneous ε_s in the bulk of the bed typically varied between 0.20 and 0.50. The gas–solid slip velocity can be quite large in the vicinity of the injection slot, though in the bulk of the bed it varied between 6 and 7 m/s. Because $v_{s,r}$ is essentially zero, v_{slip} and $v_{g,r}$ are approximately equal, and v_{slip} increases between $r = 0.25$ m and $r = 0.20$ m due to the inward radial gas flow. The concentration-based convective gas–solid mass transfer coefficient ($k_{m,c}$) can be estimated using v_{slip} and a common empirical relationship for the Sherwood number: $Sh = 2.0 + 0.6 \cdot Re_p^{1/2} \cdot Sc^{1/3}$, where Re_p is the particle-based Reynolds number and Sc is the Schmidt number. Under the conditions studied in this work, the $k_{m,c}$ values in the bed vary between 1.0 and 1.1 m/s. The validity of this simplistic expression is questionable for a dense fluidized bed; however, it indicates the potentially large interphase mass- and heat-transfer coefficients that are achievable with a GSVR.
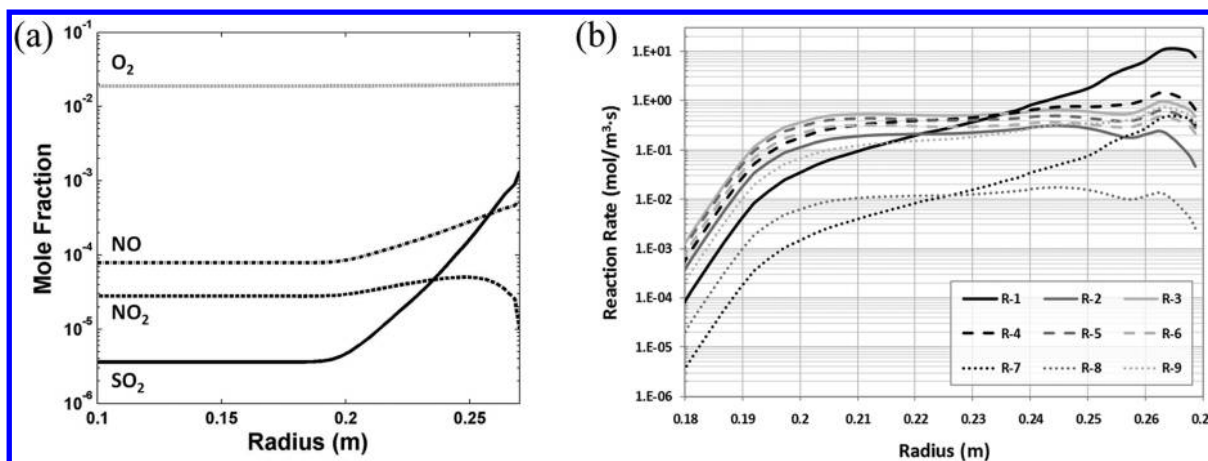
Figure 6. GSVR data for the 5.38 kg bed, single-pass case. (a) Species mole fractions as a function of radius. (b) Instantaneous rate of reaction for all reactions as a function of radius.
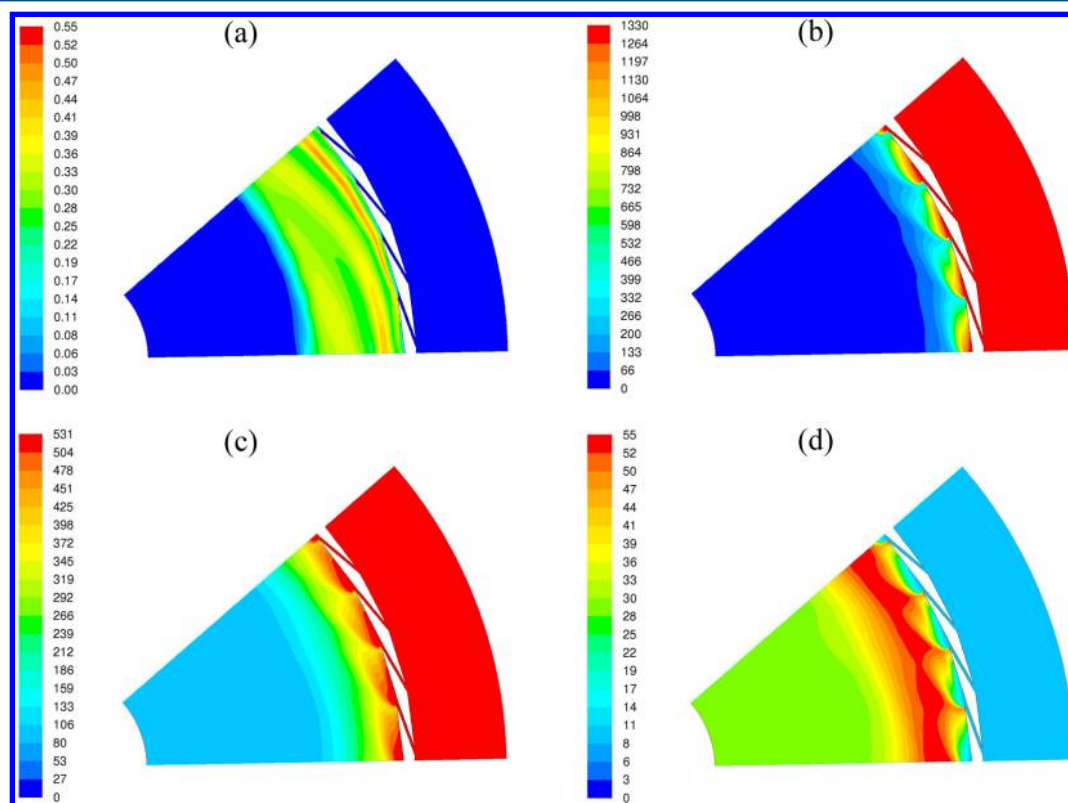

Figure 7. Instantaneous contour plots for the 5.38 kg bed, single-pass case. (a) Solids volume fraction. (b) SO_2 concentration, ppm-v. (c) NO concentration, ppm-v. (d) NO_2 concentration, ppm-v.

The mole fractions as a function of radius are presented in Figure 6a. The oxygen concentration is essentially constant because its mole fraction is at least one order of magnitude larger than the other species. Oxygen is also produced in reaction 8. The SO_2 mole fraction decreases at the fastest rate due to its relatively fast adsorption (reaction 1). Because this is a continuous, steady-state process, NO is also able to be adsorbed immediately upon entering the reactor via reaction 4. The oxidation of NO to NO_2 also contributes to the decrease in NO to a small degree. However, the oxidation of NO has a large effect on the NO_2 concentration near the injection slots because of the low initial concentration of NO_2. In the first 20 mm of bed, the oxidation of NO occurs at a faster rate than

direct (reaction 2) or indirect (reaction 8) NO_2 adsorption and causes the initial increase in the NO_2 mole fraction. Once the concentration of NO decreases sufficiently and its oxidation rate slows, the adsorption of NO_2 becomes dominant and its concentration decreases as the gas flows through the bed. The instantaneous volumetric reaction rates as a function of radius are presented in Figure 6b for the nine reactions. The reaction rates vary between approximately 0.01 and 10 mol/($m^3_{reactor}$·s). This figure presents an instantaneous snapshot of the reaction rates, and the small undulations in the rates are due to variations in ε_s. The volume-weighted average rates of reactions 1 to 9 for the entire bed are approximately 3.0, 0.21, 0.58, 0.67, 0.43, 0.31, 0.12, 0.012, and 0.32 mol/($m^3_{reactor}$·s), respectively.

The variation in reaction rates across the bed is solely due to changes in the reactant concentrations and local sorbent bulk density. The free surface site concentration does not affect the rates because it is approximately uniform. The free surface site fraction varies by approximately 0.2% between the solids feed and removal locations. This implies that the operating conditions and particle properties used in the simulation result in very efficient solids mixing within the bed. This is in agreement with qualitative observations from nonreacting flow experiments that showed a very dynamic particle behavior as the particle diameter decreased. If bed mixing was slow, a much larger variation in the free surface sites across the bed would have been observed. This also implies that the solids feed and removal locations have little effect on the overall efficiency of the unit. This was confirmed by switching the solids feed and removal locations in the simulation, which yielded similar results (not shown). The only surface species to vary significantly with position in the bed were SO_2^* and SO_2^{**}, which both varied by approximately 30% across the bed.

The instantaneous fields of ε_s and concentrations of SO_2, NO, and NO_2 are presented in Figure 7. Although these present only snapshots of dynamic observables, the fields accurately represent the steady-state process operation. The field plots show the injection plumes and the effect they have on the concentration fields. The SO_2 and NO concentrations generally decrease monotonically across the bed from the gas inlet to the freeboard region, as indicated in Figure 6a. The NO_2 concentration goes through a maximum due to the reasons discussed previously. One key aspect to note is the uniformity of the gas concentrations at the outlet of the bed and reactor. Although the injection effects cause large variations in the azimuthal cylindrical coordinate, these effects are largely damped by the time the gas flow exits the bed. This means that the outlet gas composition will be stable, which is potentially important in view of downstream processes. A typical riser may have significant variations in the outlet composition due to natural fluctuations of the multiphase flow in the riser, which can be seen in the field plots presented by Das et al.[35]

The composition of the outlet gas is summarized in Table 3, which provides the impurity mole fractions and removal efficiencies for the riser and other GSVR simulations. The GSVR with a 5.38 kg bed is calculated to be significantly more effective than the riser at removing SO_2 and NO_x. The large improvement in SO_2 removal is primarily due to the larger space−time, 160 instead of 68 kg_{solids}·s/mol in the direct comparison case, although more intimate gas−solid interaction in the GSVR also plays a role. The removal of NO and combined NO_x is also more efficient in the GSVR, although the NO_2 outlet concentration is nominally the same.

The GSVR without recycle was also simulated using 70 μm particles, which is a diameter similar to that used in the riser simulations. The particle diameter generally affects the external (via Re_p and the surface-to-volume ratio) and internal (via diffusion length) mass transfer coefficients, but it also affects bed stability in the GSVR due to differences in the drag-to-centrifugal force ratio for particles of different diameters. However, the simulation with smaller particles yielded results similar to the 200 μm case, but the removal rates are slightly higher. There are two reasons for the mostly similar results: (1) the intraparticle mass transfer resistance was assumed to be negligible in the simulations, and (2) the reactions are mainly kinetically controlled in the GSVR, which means that the external mass transfer coefficient and particle surface-to-volume ratio have a minimal effect on the net adsorption rate.

Adsorption in a GSVR with a 5.38 kg Bed and Sorbent Recycle. Simulations of a GSVR with sorbent recycled and a 5.38 kg bed were performed, and the results were nominally the same as the GSVR case with only fresh sorbent feeding. The results are summarized in Table 3. Fundamental operational differences between the GSVR and riser mean that external recycling in a GSVR has little effect on its performance, even though recycling can play a major role in the performance of a riser.

In a riser, recycling of the solids serves two purposes. First, it allows for solids at the top of the riser to be reintroduced at the bottom. In general, vertical solids mixing is limited in a riser because the gas flow rate is chosen such that particles are generally carried through the unit. Therefore, solids have little ability to flow downward, opposite the net gas flow, from the top to the bottom of the riser, i.e., internal recycling is minimal. Second, and more important, recycle in a riser is the only way to alter the solids loading and solids residence time, defined as the solids loading divided by the regenerated sorbent feed rate, in a riser for a constant gas flow rate and regeneration rate. For a constant gas inlet velocity, the average amount of solids present in the riser will depend mainly on the solids feed rate. The time it takes a particle in a riser to travel from the inlet to the outlet (the single-pass solids residence time) is primarily determined by the gas flow rate because the particles are, on average, carried by the flow at a velocity slightly less than the velocity of the gas. The axial v_{slip} was between 0.3 and 0.4 m/s for the comparison riser. However, the solids residence time in the riser can be changed by implementing recycling in the process. Recycling allows the solids loading in the riser to be increased, which essentially equates to increasing the solids volume fraction (solids loading). For example, implementing a recycle ratio of 3, as in this case, allows the solids flux to be increased from 0.54 (for fresh sorbent only) to 2.12 kg/m²·s (with recycle). The result is a much higher total solids flux with approximately the same v_s. For a constant v_g, the additional solids loading will increase the pressure drop across the riser. Additionally, complex hydrodynamics may cause the v_s field to change as ε_s increases in the riser, but this effect should be relatively small until ε_s increases significantly and is of secondary importance to the effect of the gas flow rate.

However, the solids loading in the GSVR can be set independently of the gas flow rate as long as the unit is operated below the maximum m_{bed}. The solids loading is completely determined by the initial mass loaded into the unit and the active feed and removal rates. As mentioned earlier, the GSVR also has an effective internal recycling mechanism in the form of efficient solids mixing in the bed. The external recycle loop in the GSVR provides little benefit and only has a minor effect on the bulk observables. The recycling can actually be detrimental to the stable operation of the GSVR because the recycling introduces additional momentum losses. The recycled mass has to be both slowed when removed and accelerated when injected into the unit, which results in a decrease in the v_s. A lower v_s results in less centrifugal force available to counteract drag and results in a less stable bed.

Process Intensification. One of the main benefits of the GSVR is its potential ability to intensify processes. Process intensification through the use of a GSVR can be generated via reduction in the reactor volume or via increased volumetric production/consumption rates. The reduction in reactor

Table 4. Process Intensification Summary

| | riser | GSVR simulations | | | |
		direct riser comparison	delta	5.3 kg bed w/o recycle	delta
Removal Efficiency					
SO_2 [mol/kg$_{solids}$]^a	0.21	0.21	0.5%	0.23	10%
NO_x [mol/kg$_{solids}$]^a	0.066	0.073	11%	0.074	12%
SO_2 [mol/m$^3_{reactor}$·s]	0.0086	0.93	~110×	1.02	~120×
NO_x [mol/m$^3_{reactor}$·s]	0.0027	0.33	~120×	0.33	~120×
Other Parameters					
volume (m^3)	24.2	0.23^b	~105×	0.23^b	~105×
mass transfer coefficient (m/s)	0.06–0.12	1.0–1.1		1.0–1.1	
slip velocity (m/s)	0.2–0.5	6–7		6–7	
bed pressure drop (kPa)	~0.4	~9		~17	

^{a}Defined as the moles adsorbed per second divided by the fresh sorbent feed rate to the reactors. ^{b}GSVR volume multiplied by ~10 to achieve the same gas flow rate as the riser.

volume stems from the ability to operate with a higher ε_s and/or increased reaction rates. The increase in the production/consumption rate can have different origins: (1) more efficient mass transfer may allow the net reaction rate to increase, (2) more efficient heat transfer may allow for higher reaction rates because the temperature can be controlled more effectively or the heat dissipated from the solids more efficiently, and (3) a more uniform flow pattern may result in more efficient reactor-scale gas–solid contact and less gas bypass. There is also an indirect way in which the GSVR technology may result in intensification. The increased mass/heat transfer may allow for new catalysts to be designed that will take advantage of these properties. Currently, mass-transfer-limited or heat-production-limited processes provide little incentive for the development of new and more active catalysts for use in these processes.

The process intensification potential of the GSVR was determined through a comparison with the riser. The removal efficiencies for the riser and GSVR in terms of solids loading, reactor volume, and other key operational properties are provided in Table 4. The mass transfer coefficients were determined using the aforementioned Sherwood number correlation. The GSVR with the 2.27 kg bed was determined to provide approximately equivalent SO_2 removal and a 10% improvement in NO_x removal, regardless of whether the comparison was based on the solids fed to the reactor or the solids loading. The GSVR displayed a 10–12% improvement in the removal of contaminants based on the amount of fresh sorbent fed to the reactor. The reason the NO_x removal efficiency does not increase substantially with the larger m_{bed} can be attributed to the fact that adsorbed NO_x is displaced by SO_2 (i.e., reaction 7) and converted from a surface species to a gas-phase species. On the basis of removal per reactor volume, all GSVR cases provide a large degree of intensification due to the high ε_s, and intensification factors were between 100 and 120 times that in the riser. The process intensification stems from (1) the increased solids volume fraction, (2) the increased mass transfer rates, and (3) the more uniform reactor-scale gas–solid contact. The primary fundamental disadvantage of the GSVR is the increased pressure drop, which was approximately 20 times larger than in the comparable riser. The high ΔP_{bed} is mainly attributed to the high centrifugal forces that increase the effective weight of the bed, though the high ε_s also plays a role. In high-pressure processes, the pressure drop should pose less of an operational and economic challenge.

The GSVR shows a small ability to intensify the process based on the solids loading and the amount of solids fed to the reactor; however, this is a nonideal case for showcasing the potential abilities of the GSVR. The reaction rates in the SNAP are mostly controlled by the intrinsic kinetics, and changes in the mass-transfer properties appear to have only a small effect on the net reaction rates. The volumetric impurity removal rate in the GSVR falls approximately within the "window of reality" for industrial processes, defined by P. B. Weisz to be approximately 1–10 mol/(m$^3_{reactor}$·s),[17] and is significantly larger than in the riser. To fully exploit the benefits of the GSVR, one needs to examine a test case in which mass- or heat-transfer limitations play a significant role. In this example, if the desired removal efficiency were very high, e.g. 99.99%, the GSVR would likely provide an even larger advantage over the riser as the impurity concentrations and reaction rates decreased and mass transfer limitations became much more important to the impurity removal rate. Although some clear advantages are implied in this adsorption case study, not all processes will benefit from a GSVR. Future work will continue the search for industrial processes that can benefit the most from this technology.

■ **CONCLUSIONS**

A gas–solid vortex reactor was simulated under both reacting and nonreacting flow conditions. The Eulerian–Eulerian two-fluid model showed the ability to reproduce the bulk behavior of nonreacting flows, though the fine detail observed in the experiments could not be captured. Systematic deviations were also observed in the predicted ΔP_{bed}, which indicates that ΔP_{bed} from the computational model depends too strongly on ε_s and/or the m_{bed}. New drag models may need to be derived to accurately describe the behavior of dense beds in strong centrifugal fields, especially when the mesoscale phenomena cannot be accounted for explicitly, as is the case when using the two-fluid model. It is reasonable to expect that particle clustering and other mesoscale effects will differ when operating in a force field that is ~50 times that of gravity. Despite the deficiencies, a reasonable degree of accuracy was achieved, and proof-of-principle reacting-flow calculations were performed for the SO_2/NO_x adsorption process. This work represents one of the first reacting flow calculations for gas–solid vortex reactors. These relatively mainstream CFD calculations can be used as an effective screening mechanism when searching for processes that may benefit from the increased heat and mass transfer

provided by the GSVR. Screening of processes is particularly important for guiding experimental research efforts aimed at performing bench-scale reacting-flow experiments.

The GSVR is predicted to be at least as effective as the riser in removing contaminants from a gas stream in the SNAP. For the direct comparison case, the GSVR achieved a similar degree of SO_2 removal and a ~10% increase in the NO_x removal efficiency based on the amount of solids fed to the reactor. When the sorbent m_{bed} was increased from 2.27 to 5.38 kg, the removal efficiency for SO_2 increased by ~10%, whereas the removal efficiency for NO_x only increased by a small amount based on the solids fed to the reactor. The volumetric process intensification provided by the GSVR was approximately 100−120 times the riser efficiency per unit volume of reactor. The large degree of volumetric intensification is mainly attributed to the high ε_s in the GSVR. The primary fundamental disadvantage observed in the simulation is the large ΔP_{bed} in the GSVR, though this effect may be able to be mitigated with the appropriate application choice. The GSVR continues to show promise as an industrial reactor, but significantly more effort is needed to determine the target processes that may benefit most from the unique attributes of the technology. Continued computational investigation of reacting flows and bench-scale, reacting-flow experimental setups that can provide data for direct validation of the computational models are both very important research paths needed to more rigorously evaluate the gas−solid vortex reactor concept.

ASSOCIATED CONTENT

Ⓢ Supporting Information

Justification for rate coefficient adjustment of reaction 5; additional details associated with the CFD simulations. This information is available free of charge via the Internet at http://pubs.acs.org.

AUTHOR INFORMATION

Corresponding Author
*E-mail: geraldine.heynderickx@ugent.be.

Notes
The authors declare no competing financial interest.

ACKNOWLEDGMENTS

NOTATION

H_{bed} = thickness or height of the solids bed, m
$k_{m,c}$ = convective gas−solid mass transfer coefficient, m/s
m_{bed} = mass of the solids bed or the solids loading, kg
ΔP_{bed} = pressure drop across the solids bed, kPa
ppm-v = parts per million by volume
r = radial position, m
Re_p = particle-based Reynolds number
Sc = Schmidt number
Sh = Sherwood number
v_g = gas velocity, m/s
$v_{g,t}$ = tangential component of the gas velocity, m/s
$v_{g,r}$ = radial component of the gas velocity, m/s
v_s = solids velocity, m/s

$v_{s,t}$ = tangential component of the solids velocity, m/s
$v_{s,r}$ = radial component of the solids velocity, m/s
v_{slip} = gas−solids slip velocity, m/s
β = fluid/solid momentum interaction coefficient, kg/$(m^3_{reactor}\cdot s)$
ε_s = solids volume fraction, $m^3_{solids}/m^3_{reactor}$
ρ_s = particle density for the solids phase, kg/m^3

Subscripts

recyc = associated with recycled solids
regen = associated with regenerated solids
solids = associated with total solids
reactor = associated with reactor properties

REFERENCES

(1) Anderson, L. A.; Hasinger, S. H.; Turman, B. N. 2-Component Vortex Flow Studies of Colloid Core Nuclear Rocket. *J. Spacecr. Rockets* **1972**, *9*, 311.

(2) Tang, Y. S.; Stefanko, J. S.; Dickson, P. W.; Drawbaug, Dw. Engineering Study of Colloid-Fueled Reactor Concept. *J. Spacecr. Rockets* **1971**, *8*, 129.

(3) Kochetov, L.; Sazhin, B.; Karlik, E. Experimental determination of the optimal ratios of structural dimension in the whirl chamber for drying granular material. *Khim. Neft. Mashinostr.* **1969**, *2*, 10−11.

(4) Volchkov, E. P.; Terekhov, V. I.; Kaidanik, A. N.; Yadykin, A. N. Aerodynamics and Heat and Mass-Transfer of Fluidized Particle Beds in Vortex Chambers. *Heat Transfer Eng.* **1993**, *14*, 36−47.

(5) Kuzmin, A. O.; Pravdina, M. K.; Yavorsky, A. I.; Yavorsky, N. I.; Parmon, V. N. Vortex centrifugal bubbling reactor. *Chem. Eng. J.* **2005**, *107*, 55−62.

(6) Loftus, P. J.; Stickler, D. B.; Diehl, R. C. A Confined Vortex Scrubber for Fine Particulate Removal from Flue-Gases. *Environ. Prog.* **1992**, *11*, 27−32.

(7) Ryazantsev, A. A.; Malikov, A. S.; Batoeva, A. A.; Faddeenkova, G. A. Liquid-phase oxidation of hydrogen sulphide in centrifugal bubbling apparatus. *Russ. J. Appl. Chem.* **2007**, *80*, 1544−1548.

(8) de Broqueville, A.; De Wilde, J. Numerical investigation of gas-solid heat transfer in rotating fluidized beds in a static geometry. *Chem. Eng. Sci.* **2009**, *64*, 1232−1248.

(9) De Wilde, J. New ways of fluidization in a centrifugal field. *Adv. Fluid Mech. VII* **2008**, *59*, 223−234.

(10) De Wilde, J.; de Broqueville, A. Experimental investigation of a rotating fluidized bed in a static geometry. *Powder Technol.* **2008**, *183*, 426−435.

(11) De Wilde, J.; de Broqueville, A. A rotating chimney for compressing rotating fluidized beds. *Powder Technol.* **2010**, *199*, 87−94.

(12) Dutta, A.; Ekatpure, R. P.; Heynderickx, G. J.; de Broqueville, A.; Marin, G. B. Rotating fluidized bed with a static geometry: Guidelines for design and operating conditions. *Chem. Eng. Sci.* **2010**, *65*, 1678−1693.

(13) Nakamura, H.; Tokuda, T.; Iwasaki, T.; Watano, S. Numerical analysis of particle mixing in a rotating fluidized bed. *Chem. Eng. Sci.* **2007**, *62*, 3043−3056.

(14) Quevedo, J.; Pfeffer, R.; Shen, Y. Y.; Dave, R.; Nakamura, H.; Watano, S. Fluidization of nanoagglomerates in a rotating fluidized bed. *AIChE J.* **2006**, *52*, 2401−2412.

(15) Sazhin, B. S.; Kochetov, L. M.; Belousov, A. S. Retention capacities and flow patterns of vortex contactors. *Theor. Found. Chem. Eng.* **2008**, *42*, 125−135.

(16) Volchkov, E. P.; Dvornikov, N. A.; Yadykin, A. N. Characteristic features of heat and mass transfer in a fluidized bed in a vortex chamber. *Heat Transf. Res.* **2003**, *34*, 486−98.

(17) Weisz, P. B. The Science of Possible: Windows on Reality. *CHEMTECH* **1982**, *12*, 424−425.

(18) Qian, G. H.; Bagyi, I.; Pfeffer, R.; Shaw, H.; Stevens, J. G. A parametric study of a horizontal rotating fluidized bed using slotted

and sintered metal cylindrical gas distributors. *Powder Technol.* **1998**, *100*, 190−199.

(19) Takahashi, T.; Tanaka, Z.; Itoshima, A.; Fan, L. T. Performance of a Rotating Fluidized-Bed. *J. Chem. Eng. Jpn.* **1984**, *17*, 333−336.

(20) Watano, S.; Nakamura, H.; Hamada, K.; Wakamatsu, Y.; Tanabe, Y.; Dave, R. N.; Pfeffer, R. Fine particle coating by a novel rotating fluidized bed coater. *Powder Technol.* **2004**, *141*, 172−176.

(21) Nakamura, H.; Watano, S. Numerical simulation of particle fluidization behaviors in a rotating fluidized bed. *Stud. Surf. Sci. Catal.* **2006**, *159*, 505−508.

(22) Trujillo, W. R.; De Wilde, J. Computational Fluid Dynamics Simulation of Fluid Catalytic Cracking in a Rotating Fluidized Bed in a Static Geometry. *Ind. Eng. Chem. Res.* **2010**, *49*, 5288−5298.

(23) Staudt, N.; De Broqueville, A.; Trujillo, W. R.; De Wilde, J. Low-Temperature Pyrolysis and Gasification of Biomass: Numerical Evaluation of the Process Intensification Potential of Rotating- and Circulating Rotating Fluidized Beds in a Static Fluidization Chamber. *Int. J. Chem. Reactor Eng.* **2011**, *9*, 10.1515/1542-6580.2459.

(24) *Handbook of Polymer Reaction Engineering*; Wiley-VCH Verlag GmbH & Co.: Germany, 2005; Vol. 1.

(25) Bharadwaj, S. S.; Schmidt, L. D. Synthesis Gas-Formation by Catalytic-Oxidation of Methane in Fluidized-Bed Reactors. *J. Catal.* **1994**, *146*, 11−21.

(26) Goetsch, D. A.; Schmidt, L. D. Microsecond catalytic partial oxidation of alkanes. *Science* **1996**, *271*, 1560−1562.

(27) Goetsch, D. K.; Witt, P. M.; Schmidt, L. D. Partial oxidation of butane at microsecond contact times. *Heterog. Hydrocarbon Oxid.* **1996**, *638*, 124−139.

(28) Huff, M.; Schmidt, L. D. Partial Oxidation and Cracking of Alkanes over Noble-Metal Coated Monoliths. *Abstr. Pap. Am. Chem. Soc.* **1994**, *207*, 68-CATL.

(29) Torniainen, P. M.; Chu, X.; Schmidt, L. D. Comparison of Monolith-Supported Metals for the Direct Oxidation of Methane to Syngas. *J. Catal.* **1994**, *146*, 1−10.

(30) Deutschmann, O.; Schmidt, L. D. Modeling the partial oxidation of methane in a short-contact-time reactor. *AIChE J.* **1998**, *44*, 2465−2477.

(31) Faravelli, T.; Goldaniga, A.; Ranzi, E.; Dietz, A.; Davis, M.; Schmidt, L. D. Partial oxidation of hydrocarbons: An experimental and kinetic modeling study. *Natural Gas Convers. V* **1998**, *119*, 575−580.

(32) Iordanoglou, D. I.; Schmidt, L. D. Oxygenate formation from n-butane oxidation at short contact times: Different gauze sizes and multiple steady states. *J. Catal.* **1998**, *176*, 503−512.

(33) Schmidt, L. D.; Deutschmann, O.; Goralski, C. T. Modeling the partial oxidation of methane to syngas at millisecond contact times. *Natural Gas Convers. V* **1998**, *119*, 685−692.

(34) Schmidt, L. D.; Hohn, K. L.; Davis, M. B. Catalytic partial oxidation of methane at extremely short contact times: Production of acetylene. *Natural Gas Convers. V* **1998**, *119*, 397−402.

(35) Das, A. K.; De Wilde, J.; Heynderickx, G. J.; Marin, G. B. CFD simulation of dilute phase gas-solid riser reactors: Part II - Simultaneous adsorption of SO_2-NO_x from flue gases. *Chem. Eng. Sci.* **2004**, *59*, 187−200.

(36) *ANSYS FLUENT Theory Guide, Release 13.0*; ANSYS, Inc.: Canonsburg, PA, 2010.

(37) Johnson, P. C.; Jackson, R. Frictional Collisional Constitutive Relations for Antigranulocytes-Materials, with Application to Plane Shearing. *J. Fluid Mech.* **1987**, *176*, 67−93.

(38) *ANSYS FLUENT User's Guide, Release 13.0*; ANSYS, Inc.: Canonsburg, PA, 2010.

(39) Shih, T. H.; Liou, W. W.; Shabbir, A.; Yang, Z. G.; Zhu, J. A New Kappa-Epsilon Eddy Viscosity Model for High Reynolds-Number Turbulent Flows. *Comput. Fluids* **1995**, *24*, 227−238.

(40) Moysey, P. A.; Thompson, M. R. Determining the collision properties of semi-crystalline and amorphous thermoplastics for DEM simulations of solids transport in an extruder. *Chem. Eng. Sci.* **2007**, *62*, 3699−3709.

(41) Fuller, E. N.; Schettle, Pd.; Giddings, J. C. A New Method for Prediction of Binary Gas-Phase Diffusion Coefficients. *Ind. Eng. Chem.* **1966**, *58*, 19.

(42) Das, A. K.; De Wilde, J.; Heynderickx, G. J.; Marin, G. B.; Iversen, S. B.; Felsvang, K. Simultaneous adsorption of SO_2-NO_x from flue gases in a riser configuration. *AIChE J.* **2001**, *47*, 2831−2844.

(43) Das, A. K.; De Wilde, J.; Heynderickx, G. J.; Marin, G. B.; Vierendeels, J.; Dick, E. CFD simulation of dilute phase gas-solid riser reactors: Part I - A new solution method and flow model validation. *Chem. Eng. Sci.* **2004**, *59*, 167−186.

(44) De Wilde, J.; Das, A. K.; Heynderickx, G. H.; Marin, G. B. Development of a transient kinetic model for the simultaneous adsorption of SO_2-NO_x over Na/gamma-Al_2O_3 sorbent. *Ind. Eng. Chem. Res.* **2001**, *40*, 119−130.

(45) Ekatpure, R. P.; Suryawansh, V.; Heynderickx, G. J.; de Broqueville, A.; Marin, G. B. Experimental Investigation of a Gas-Solid Rotating Bed Reactor with Static Geometry. *Chem. Eng. Process.: Process Intensification* **2011**, *50*, 77−84.

(46) Benyahia, S.; Syamlal, M.; O'Brien, T. J. Extension of Hill-Koch-Ladd drag correlation over all ranges of Reynolds number and solids volume fraction. *Powder Technol.* **2006**, *162*, 166−174.

(47) Beetstra, R.; van der Hoef, M. A.; Kuipers, J. A. M. Drag force of intermediate Reynolds number flow past mono- and bidisperse arrays of spheres. *AIChE J.* **2007**, *53*, 489−501.

875

dx.doi.org/10.1021/ie300399w | *Ind. Eng. Chem. Res.* 2013, 52, 861−875